Ain Shams Engineering Journal 11 (2020) 727–739

Contents lists available at ScienceDirect

Ain Shams Engineering Journal

journal homepage: www.sciencedirect.com

Civil Engineering

# Effects of water depth, mooring line diameter and hydrodynamic coefficients on the behaviour of deepwater FPSOs

Montasir Osman Ahmed Ali *, Idris Ahmed Ja'e, Matthew Guan Zhen Hwa

*Department of Civil and Environmental Engineering, Universiti Teknologi PETRONAS, Bandar Seri Iskandar, Perak 32610, Malaysia*

ARTICLE INFO

*Article history:*
Received 26 April 2018
Revised 15 October 2019
Accepted 5 December 2019
Available online 30 December 2019

*Keywords:*
Coupled dynamic analysis
FPSO
Deepwater
Mooring line
Motions
Mooring line tensions

ABSTRACT

Floating Production Storage and Offloading (FPSO) platforms are the most used floating structures in the offshore oil and gas industry. They are generally kept in place with the aid of mooring lines anchored to the seabed. In deep waters, the responses of mooring lines become more significant and difficult to be accurately captured through experiments or numerical quasi-static models. Thus, this paper assesses the influence of water depth, mooring line diameter as well as added inertia and drag coefficients on the behaviour of a deepwater turret-moored FPSO platform. The commercial software, AQWA, is used to conduct fully coupled time-domain dynamic analysis for the FPSO subjected to a unidirectional random wave. The results highlighted the influence of water depths and mooring line diameter in reducing surge motions and increasing mooring line tensions, at the same time furnishes valid information on the fluctuation trend of these responses. Drag and inertia coefficients were found to have little impact on the dynamic motions of FPSO.



## 1. Introduction

Floating platforms are commonly deployed in offshore deepwater regions for the exploration and production of oil and gas. FPSO, in particular, has many advantages which include providing a better option for smaller oil field where the possibility of depleting the reserve is within a couple of years. While in operation, they can be utilized for Extended Well Testing (EWT) and pilot production to gather important reservoir data [1,2]. They are held in place by an arrangement of mooring lines anchored to the seabed. These mooring lines contribute toward the floating system's damping, which in turn influence its dynamic motions and mooring line tensions.

In shallow waters, the mooring induced damping is considered insignificant. Research has shown that in relatively shallow water depths, the effects can be ignored while still obtaining reasonably accurate results [3]. In such cases, quasi-static analysis or uncoupled analysis, which are computationally inexpensive can be applied.

Moreover, physical model testing of a complete scaled-down model may be carried out for such systems operating in relatively shallow water depth. This is generally acknowledged as the most reliable method of testing a system. Numerical simulations are typically validated against physical model test results before further analysis [4].

At greater water depths, however, the damping, as well as added mass from the mooring lines, become too significant to be ignored. Experimental tests of a complete system with its mooring lines in deep and ultra-deep waters is limited by the existing wave facilities available due to their relatively shallow basin depth, making it difficult to model platforms in deep waters within the typical scale size (between 1:40 to 1:100). On the other hand, accurate prediction of the system may not be possible using the relatively simple quasi-static approach, because the method ignores the damping effects of the mooring lines. Studies have found significant discrepancies in the low-frequency surge motion [5] as well as in the mooring line tensions [6,7].

Hence, to accurately predict the dynamic responses of floating platform operating in deepwater, researchers often employ numerical simulations using fully coupled dynamic analysis. The method considers the simultaneous interaction of the platform motion and mooring line dynamics. Studies have been conducted to

* Corresponding author.
*E-mail addresses:* montasir.ahmedali@utp.edu.my (M.O. Ahmed Ali), idris_18001528@utp.edu.my (I.A. Ja'e), matthew.guan_g03190@utp.edu.my (M.G. Zhen Hwa).

Peer review under responsibility of Ain Shams University.

Production and hosting by Elsevier

https://doi.org/10.1016/j.asej.2019.12.001
2090-4479/

benchmark coupled dynamic analysis against uncoupled quasi-static analysis method [8,9] as well as a truncated model test [10]. The results showed that the uncoupled approach and truncated model test tend to overpredict both the low-frequency responses and the mooring line tensions. Hence, this justifies the need for coupled dynamic analysis in accurately estimating floating system behaviour.

In order to investigate the effect of mooring line damping on the low-frequency motions of a floating vessel, Wichers and Huijsmans presented a numerical model which calculates the cable dynamics by discretising the mooring line to a finite number of nodes [11]. Dynamic analysis using finite element method (FEM) has since been in use for rigorous and accurate predictions of floating systems. Chen developed a coupled numerical simulation code called COUPLE [12], which is capable of analysing nonlinear dynamic responses in 6 degrees of freedom (DOF) for spars and TLPs. A similar code, WINPOST was developed by Ran to analyse the dynamic behaviour of floating structures together with their mooring system [13]. The code was later modified by Arcandra for the analysis of turret-moored FPSO systems [14]. Kim further expanded on the code to include multiple floating systems coupled with their mooring lines and risers [15].

Detailed investigations with respect to the effects of water depths were conducted by Lin and Sayer by means of a moored system at depths ranging from 300 to 3000 m [16,19,20]. Result of the studies reveals that surge motion and mooring line tensions are primarily governed by low frequency (LF) responses, and are prominent at greater water depths. The authors strongly recommend fully coupled time-domain dynamic analysis for depths greater than 1000 m, in order to incorporate the nonlinearities and coupling effects of the mooring and riser system.

Studies [17] have consistently shown that the low-frequency responses of a floating platform and its mooring lines are particularly sensitive to water depth. The mean offset and low-frequency horizontal motions tend to significantly increase at greater depths, thought to be mainly attributed to the decreasing horizontal stiffness of the mooring system.

This study further explores the influence of water depth on the dynamic response of FPSO for different mooring diameters, as well as the effects of drag and added inertia coefficients.

A turret-moored FPSO is taken as a case study. The Commercial software AQWA is used to numerically model the FPSO and conduct a fully coupled dynamic analysis simulations. Prior to the analysis, the AQWA numerical model was validated against published results of an experimental as well as a numerical simulation [18]. The validation was conducted for an FPSO operating in deepwater under the action of wind, wave, and current environment. The AQWA model was generally found to be within reasonable agreement particularly with the published numerical data. The study focuses on water depths between 1000 and 2000 m.

Performing evaluation of forces in the mooring lines of an FPSO is in strong connection with the level of the dynamicity of its behaviour. In this respect, various parameters and methods of analysis of floating platforms have been studied in trying to assess the influence of mooring lines and/or risers on the behaviour of a floating system [9,19]. Some studies conducted provide a general assessment on the behaviour of a floating platform and its mooring lines and risers in different water depths, while focusing on other aspects in their work [5,20]. Hybrid tests, involving experimental approaches and techniques were carried out to study the influence of migration from deep to very deep water (>1000 m) of floating platform [21].

Detailed investigations were conducted by Lin and Sayer by means of a moored system at depths ranging from 300 to 3000 m [22,23] it was highlighted in the studies that surge motion and mooring line tensions are primarily governed by low frequency (LF) responses, and are prominent at greater water depths. The authors strongly recommend the fully coupled time-domain analysis for water depths greater than 1000 m, in order to incorporate the nonlinearities and coupling effects of the mooring and riser system.

In the same vein, Heurtier et al. [16] reported the outcome of a coupled analysis at 2000 m that the surge motion FPSO was also greater at low frequency, further reiterating the influence of water depth. Mooring diameter was reported to have a significant influence on the cumulative payload on the exerted on the FPSO hull as well as the line length [24].

## 2. FPSO configurations and mooring lines' properties

Numerical simulations using a fully coupled dynamic analysis method were carried out using the commercial software AQWA, utilizing the first-order potential theory for radiation and diffraction analysis [25]. Summarized process of the analysis is presented in Fig. 1. Computations of the hull hydrodynamics were done via 3D radiation/diffraction analysis and solved by means of Quadratic transfer function (QTF) method. The simulations were carried out in time-domain.

In this paper, a turret moored FPSO is considered as a case study. The design of the hull is based on the model by Kim et al. [26] and is shown in Table 1.

The FPSO is connected to a mooring system comprising of 12 lines. The lines are divided into four groups, i.e. G1, G2, G3 and G4, with three lines in each group. The line arrangements are as depicted in Fig. 2 while mooring line properties for the polyester and chain segments are shown in Table 2.

An attempt was made to keep the mooring lines arrangement for all water depth cases as close as possible to the system at 2000 m depth (i.e. at approximately the same inclination angle from the bottom of the seabed to the turret). Fig. 3 provides visualization on the steps taken to achieve the above requirement, as suggested by [27], by adjusting mooring line segments' length and introducing clump weights. Additional segments were also added, which extends the mooring line to lie on the seabed. These additional segments function only to achieve the required surge mooring line restoring force. Table 3 lists the mooring line pretension as well as the length of each segment suspended above the seabed.

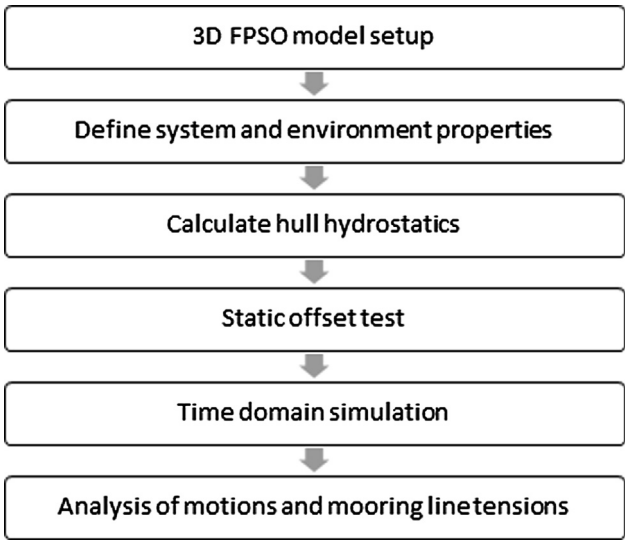


**Fig. 1.** Numerical simulation process.

**Table 1**
FPSO details.

| Parameter | Units | Value |
|---|---|---|
| Production level | bpd | 120,000 |
| Storage | bbls | 1,440,000 |
| Vessel size | kDWT | 200 |
| Length between perpendicular, Lpp | m | 310 |
| Breadth | m | 47.17 |
| Height | m | 28.04 |
| Draft (80% loaded) | m | 15.121 |
| Displacement | MT | 186,051 |
| Surge centre of gravity from turret, CGx | m | −109.67 |
| Heave centre of gravity from mean water level, CGx | m | −1.8 |
| Frontal wind area | $m^2$ | 4209.6 |
| Transverse wind area | $m^2$ | 16018.6 |
| Roll radius of gyration at CG, Rxx | m | 14.036 |
| Sway radius of gyration at CG, Ryy | m | 77.47 |
| Yaw radius of gyration at CG, Rzz | m | 79.3 |
| Turret in center line behind Fpp | m | 38.75 |
| Turret diameter | m | 15.85 |

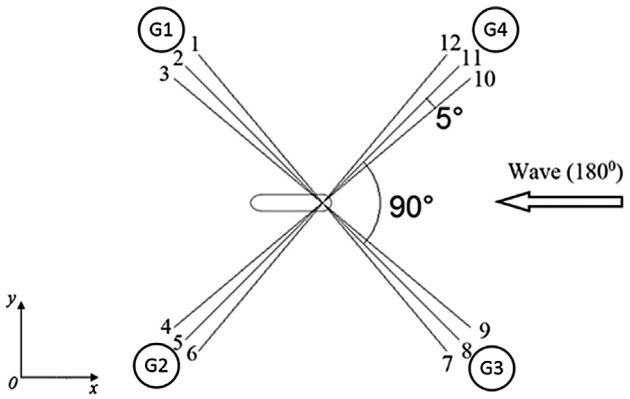


**Fig. 2.** Mooring arrangement.

## 3. Governing equations

### 3.1. Wave force formulation

The fluid was assumed to be inviscid, incompressible, irrotational and in a continuous flow, hence the fluid motion is expressed using the Laplace equation,

$$\Delta\varphi = \frac{\partial^2\varphi}{\partial x^2} + \frac{\partial^2\varphi}{\partial y^2} + \frac{\partial^2\varphi}{\partial z^2} = 0 \tag{1}$$

where $\varphi$ is the velocity potential which could be defined in terms of wave-particle velocities, i.e. $u$, $v$ and $w$, as in Eq. (2).

$$u = \frac{\partial\varphi}{\partial x}; \quad v = \frac{\partial\varphi}{\partial z}; \quad w = \frac{\partial\varphi}{\partial y} \tag{2}$$

The first-order velocity potential is expressed in Eq. (3),

$$\varphi_1 = \frac{ag}{\omega}\frac{\cosh ks}{\cosh kd}\sin\theta \tag{3}$$

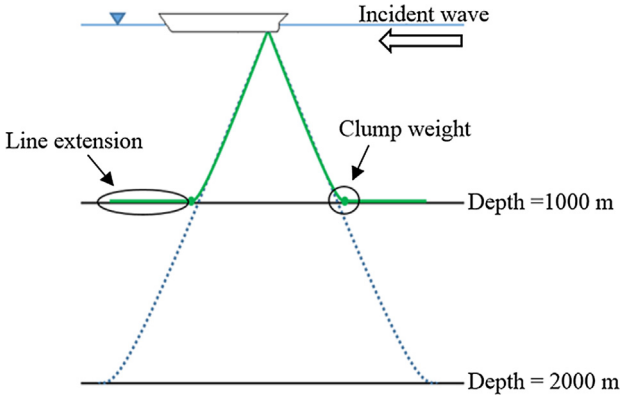


**Fig. 3.** Mooring line inclination (side view).

where:

$a$ = wave amplitude, $g$ = acceleration due to gravity, $\omega$ = wave frequency, $s$ = effective water depth, $d$ = water depth, $\theta = kx - \omega t$.

The FPSO platform is subjected to the wave condition shown in Table 4. Current and wind are not considered in this study. A unidirectional random wave is considered, propagating in the direction from the vessel bow (where the turret is located) to stern. The JONSWAP spectrum model was adopted, given as:

$$S(\omega) = \frac{\propto g^2\gamma^2}{\omega^5} exp\left(-\frac{(5_{\omega_p}{}^4)}{4\omega^4}\right) \tag{4}$$

where, $\omega_p$ =peak frequency, $\gamma$ = peak enhancement factor and $\alpha$ = constant relating the wind speed (0.0081).

The total velocity potential due to incident ($\varphi_I$), radiation ($\varphi_R$) and diffraction ($\varphi_D$) waves can, therefore, be expressed as:

$$\varphi\left(\vec{X}\right)e^{-i\omega t} = \left[(\varphi_I + \varphi_D) + \sum_{j=1}^{6}\varphi_{rj}x_j\right]e^{-i\omega t} \tag{5}$$

where $\vec{X} = (X, Y, Z)$ = location of a point on the body, $\varphi_{rj}$ = radiation wave potential due to the motion in $j$ direction and $x_j$ = motion in $j$ direction.

The incident wave velocity potential can be inferred from the following equation:

$$\varphi_I\left(\vec{X}\right)e^{-i\omega t} = -\frac{iga_w}{\omega}\frac{\cosh ks}{\cosh kd}e^{i[-\omega t + k(X\cos\chi + Y\cos\chi) + \varepsilon]} \tag{6}$$

Eqs. (7) and (8) are the equations of diffraction and radiation potentials respectively.

$$\frac{\partial\varphi_D^{(1)}}{\partial n} = -\frac{\partial\varphi_I^{(1)}}{\partial n} \tag{7}$$

$$\frac{\partial\varphi_R^{(1)}}{\partial n} = -i\omega n.\left(\xi|^{(1)} + \alpha^{(1)} \times r\right) \tag{8}$$

where $\xi$ is the amplitude of translational motion (surge, sway and heave), $\alpha$ stands for the amplitude of rotational motion of the plat-

**Table 2**
Mooring line properties.

| Parameter | Units | Value | | | | |
|---|---|---|---|---|---|---|
| | | Polyester | | | | Chain |
| Diameter | mm | 156 | 201 | 251 | 290 | 95.3 |
| Mass per unit length | kg/m | 16.7 | 28.3 | 44.2 | 59.2 | 189.2 |
| Stiffness, EA | kN | 187,000 | 321,000 | 509,000 | 670,000 | 820,900 |
| Normal drag coefficient, $C_{DN}$ | – | 1.2 | 1.2 | 1.2 | 1.2 | 2.45 |
| Normal added inertia coefficient, $C_{IN}$ | – | 1.1 | 1.1 | 1.1 | 1.1 | 2 |

**Table 3**
Mooring line pretension and suspended length.

| Polyester diameter (mm) | Depth (m) | Pretension (kN) | Line segment (m) | | |
|---|---|---|---|---|---|
| | | | Top | Middle | Bottom |
| 156 | 1000 | 589 | 121.9 | 1327.5 | – |
| | 1100 | 585 | 121.9 | 1474.6 | – |
| | 1200 | 612 | 121.9 | 1621 | – |
| | 1300 | 601 | 121.9 | 1758.25 | 10 |
| | 1400 | 644 | 121.9 | 1893.9 | 20 |
| | 1500 | 896 | 121.9 | 1968 | 90.25 |
| | 1600 | 1078 | 121.9 | 2092.5 | 110 |
| | 1700 | 1283 | 121.9 | 2216.25 | 130 |
| | 1800 | 1397 | 121.9 | 2360.5 | 130 |
| | 1900 | 1330 | 121.9 | 2487 | 150 |
| | 2000 | 1429 | 121.9 | 2689.4 | 91.4 |
| 201 | 1000 | 611 | 121.9 | 1327.6 | – |
| | 1100 | 622 | 121.9 | 1474 | – |
| | 1200 | 617 | 121.9 | 1621.25 | – |
| | 1300 | 653 | 121.9 | 1767.6 | – |
| | 1400 | 688 | 121.9 | 1914.1 | – |
| | 1500 | 708 | 121.9 | 2060.75 | – |
| | 1600 | 734 | 121.9 | 2207.4 | – |
| | 1700 | 758 | 121.9 | 2354.1 | – |
| | 1800 | 783 | 121.9 | 2500.8 | – |
| | 1900 | 827 | 121.9 | 2647.1 | – |
| | 2000 | 840 | 121.9 | 2794.1 | – |
| 251 | 1000 | 633 | 121.9 | 1328 | – |
| | 1100 | 658 | 121.9 | 1474 | – |
| | 1200 | 694 | 121.9 | 1621 | – |
| | 1300 | 749 | 121.9 | 1767 | – |
| | 1400 | 767 | 121.9 | 1914 | – |
| | 1500 | 810 | 121.9 | 2061 | – |
| | 1600 | 852 | 121.9 | 2208 | – |
| | 1700 | 889 | 121.9 | 2354 | – |
| | 1800 | 941 | 121.9 | 2500.3 | – |
| | 1900 | 986 | 121.9 | 2646.7 | – |
| | 2000 | 1016 | 121.9 | 2793.6 | – |
| 290 | 1000 | 675 | 121.9 | 1327.6 | – |
| | 1100 | 728 | 121.9 | 1474 | – |
| | 1200 | 775 | 121.9 | 1620.5 | – |
| | 1300 | 821 | 121.9 | 1766.6 | – |
| | 1400 | 871 | 121.9 | 1914.4 | – |
| | 1500 | 927 | 121.9 | 2061 | – |
| | 1600 | 963 | 121.9 | 2206.75 | – |
| | 1700 | 1029 | 121.9 | 2354 | – |
| | 1800 | 1092 | 121.9 | 2500.25 | – |
| | 1900 | 1146 | 121.9 | 2646.7 | – |
| | 2000 | 1220 | 121.9 | 2793.6 | – |

**Table 4**
Environmental condition.

| Parameter | Units | Value |
|---|---|---|
| Water depth | m | 1829 |
| Wave | | |
| Significant wave height, $H_s$ | m | 12.19 |
| Peak period, $T_p$ | s | 14 |
| Spectrum | JONSWAP | – |
| Peak factor, γ | – | 2.5 |
| Direction | $^0$ | 180 |

form (roll, pitch and yaw), *r* is the position vector, while n is the outward unit normal vector on the body surface. Thus, the six degrees of freedom can be represented as:

$$x_j = \begin{cases} \xi_j^{(1)} & for\ j = 1,2,3 \\ \alpha_{j-3}^{(1)} & for\ j = 4,5,6 \end{cases} \tag{9}$$

The generalised expression of radiation potential is shown in Eq. (10),

$$\varphi_R^{(1)} = \sum_{j=1}^{6} \varphi_j^{(1)} x_j \tag{10}$$

where $\varphi_j^{(1)}$ is the velocity potential of rigid body motion with unit amplitude in the *jth* mode when the incident wave does not exist.

The 1st order dynamic pressure distribution can be computed using the linearized Bernoulli equation:

$$p^{(1)} = -\rho \frac{\partial \Phi\left(\vec{X}, t\right)}{\partial t} = i\omega\rho\varphi\left(\vec{X}\right)e^{-i\omega t} \tag{11}$$

where $\rho$ is the fluid density.

The 1st order hydrodynamic forces on the body can then be written in the generalised form as:

$$F_j e^{-i\omega t} = -\int_{S_0} p^{(1)} n_j dS = \left[-i\omega\rho \int_{S_0} \varphi\left(\vec{X}\right) n_j dS\right] e^{-i\omega t} \tag{12}$$

Combining Eqs. (5) and (12), the 1st order wave force can be expressed as:

$$F_j = \left[\left(F_{Ij} + F_{Dj}\right) + \sum_{k=1}^{6} F_{Rjk} x_k\right] e^{-i\omega t}, \quad j = 1,6 \tag{13}$$

where:

Froude-Krylov force due to an incident wave,

$$F_{Ij} = -i\omega\rho \int_{S_0} \varphi_I(\vec{X}) n_j dS \tag{14}$$

Diffraction force due to diffracting wave

$$F_{Dj} = -i\omega\rho \int_{S_0} \varphi_D\left(\vec{X}\right) n_j dS \tag{15}$$

Radiation force due to radiating wave induced by the $k^{th}$ body motion

$$F_{rjk} = -i\omega\rho \int_{S_0} \varphi_{Rk}\left(\vec{X}\right) n_j dS \tag{16}$$

The added mass and damping coefficients can be obtained from $F_{rjk}$ by expressing the radiation velocity potential in the complex form:

$$\begin{aligned} F_{rjk} &= -i\omega\rho \int_{S_0} \left\{Re\left[\varphi_{rk}\left(\vec{X}\right)\right] + i\mathrm{ln}\left[\varphi_{rk}\left(\vec{X}\right)\right]\right\} n_j dS \\ &= \omega\rho \int_{S_0} \mathrm{ln}\left[\varphi_{rk}\left(\vec{X}\right)\right] n_j dS - i\omega\rho \int_{S_0} Re\left[\varphi_{rk}\left(\vec{X}\right)\right] n_j dS \end{aligned} \tag{17}$$

### 3.2. Dynamics of mooring lines

AQWA software uses the discrete lump-mass model in solving mooring line responses. The effects of line mass, drag, inline elastic tension and bending moment are considered

In analysing the mooring lines, assuming no torque or twisting moment, equation of motion of the mooring line can be written as:

$$\frac{\partial \vec{T}}{\partial S_e} + \frac{\partial \vec{V}}{\partial S_e} + \vec{w} + \vec{F}_h = m\frac{\partial^2 \vec{R}}{\partial t^2} \tag{18}$$

where $\vec{T}$ = tension at the first node of the element, $\vec{V}$ = shear force at the first node of the element, $\vec{w}$ = element weight per unit length, $\vec{F}_h$ = external force per unit length, $m$ = structural mass per unit length, $\vec{R}$ = positon at the first node of the element, and $S_e$ = cable length.

The total gravitational forces at nodes j and j + 1 are expressed in a 6 × 1 matrix, given as:

$$\mathbf{w} = \left(\vec{w}_j,\ \vec{w}_{j+1}\right)^T = \left\{\ 0,\ \ 0,\ \ -\tfrac{1}{2}(mL_j + M)g,\ \ \ 0,\ \ 0,\ \ -\tfrac{1}{2}mL_jg\ \right\}^T \tag{19}$$

where $L_j$ = unstretched element length.

The wave excitation force is ignored on the dynamic cable; thus the hydrodynamic force ($F_{hd}$) is the summation of the buoyant force ($F_b$), drag force ($F_D$) and added mass radiation force ($F_a$):

$$F_{hd} = F_b + F_D + F_a \tag{20}$$

$$\mathbf{F}_{hd} = \mathbf{F}_b + \mathbf{F}_D - \mathbf{m}_a\left[\ \vec{a}_j,\ \ \vec{a}_{j+1}\ \right]^T \tag{21}$$

where $\vec{a}_j$ = acceleration at node $j$.

The element buoyant force matrix is expressed as:

$$\mathbf{F}_b = \left\{\ 0,\ \ 0,\ \ \tfrac{1}{2}\rho A_{cj}L_jg,\ \ \ 0,\ \ 0,\ \ \tfrac{1}{2}\left(\rho A_{cj}L_j + M_b\right)g\ \right\}^T \tag{22}$$

where $A_{cj}$ = equivalent cross-sectional area, and $M_b$ = mass of buoy.

The time-dependent drag force of an element is given by Eq. (23).

$$\mathbf{F}_d(t) = \left\{\begin{array}{c} \mathbf{f}_d(j) - \tfrac{1}{2}C_{dc}S_c\rho_w\left|\mathbf{U}_j(t) - \mathbf{V}_j(t)\right|\left\{\mathbf{U}_j(t) - \mathbf{V}_j(t)\right\} \\ \mathbf{f}_d(j+1) - \tfrac{1}{2}C_{db}S_b\rho_w\left|\mathbf{U}_{j+1}(t) - \mathbf{V}_{j+1}(t)\right|\left\{\mathbf{U}_{j+1}(t) - \mathbf{V}_{j+1}(t)\right\} \end{array}\right\} \tag{23}$$

where $C_{dc}$ = drag coefficient of clump weight, $C_{db}$ = drag coefficient of intermediate buoy, $S_c$ = surface area of clump weight, $S_b$ = surface area of intermediate buoy, $\mathbf{U}_j$ = structural velocity matrix at $j$, and $\mathbf{V}_j$ = current velocity matrix at $j$.

Segment tension is determined using (24) as presented in [28].

$$T^{k+1}(\tau + \Delta\tau) = T^k(\tau + \Delta\tau) - [\Delta\psi(\tau)]^{-1}\psi^k(\tau) \tag{24}$$

Where $\psi$ = segment length error vector, $T^k$= tentative segment tension vector at the *k-th* iteration, $\Delta\psi$= length error derivative matrix.

For each time step, the system of equation is solved until an acceptable convergence of $T^{k+1}(\tau + \Delta\tau)$ is obtained. Tentative tension is used as initial tension in the previous step. Each node $j$ is connected to the adjacent nodes $j-1$ and $+1$.

### 3.3. Equation of motion

The six-degree of freedom (6DOF) motion of the FPSO, otherwise known as the centroidal displacement in the $x, y, z$ plane is represented by equilibrium equation of motion relating the structural motion and the resultant of force vector (in this case, only wave), total radiation force, and total force from mooring lines. For each of the DOF, the motion of the structure in one direction is associated with added mass and damping term in that direction and the other directions as well.

The equation of motion is of the platform is given as:

$$[M]\left\{\frac{\partial x_G^2}{\partial t^2}\right\} + [C]\left\{\frac{\partial x_G}{\partial t}\right\} + [K]\{x_G\} = F(t) \tag{25}$$

where, $[M] = [m + m_a]$, $m$ is the system structural mass, and $m_a$ is the added mass component in infinite frequency. **C** is the damping coefficient, and K is the system stiffness consisting of contributions from the hydrostatic stiffness and mooring stiffness, $x_G$ is the structural displacement in the six degrees of freedom considered, $\frac{\partial x_G}{\partial t}$ is the structural velocity vector, while $\frac{\partial x_G^2}{\partial t^2}$ is the structural acceleration vector. Eqs. (26)–(29) show the structural mass, added mass, hydrostatic and mooring line stiffness matrices respectively.

$$[m] = \begin{bmatrix} m & 0 & 0 & 0 & mz_G & -my_G \\ 0 & m & 0 & -mz_G & 0 & mx_G \\ 0 & 0 & m & my_G & -mx_G & 0 \\ 0 & -mz_G & my_G & I_{11} & I_{12} & I_{13} \\ mz_G & 0 & -mx_G & I_{21} & I_{22} & I_{23} \\ -my_G & mx_G & 0 & I_{31} & I_{32} & I_{33} \end{bmatrix} \tag{26}$$

$m$ is the mass of the platform with the centre of gravity at $x_B, y_G, z_G$.

$$[m_a] = \begin{bmatrix} m_{11} & 0 & m_{13} & 0 & m_{15} & 0 \\ 0 & m_{22} & 0 & m_{24} & 0 & m_{26} \\ m_{31} & 0 & m_{33} & 0 & m_{35} & 0 \\ 0 & m_{42} & 0 & m_{44} & 0 & m_{46} \\ m_{51} & 0 & m_{53} & 0 & m_{55} & 0 \\ 0 & m_{62} & 0 & m_{64} & 0 & m_{66} \end{bmatrix} \tag{27}$$

Eq. (27) is a reduced form of the original matrix consisting of 36 components after eliminating added mass due to the symmetry of FPSO, component of the added mass matrix is as shown in Table 5 as given by [29]. That is, $m_{ij}\delta_{ij}$ , where, $m_{ij} = m_{ji}$ considering the Kronecker delta function, $\delta_{ij} = \left\{\begin{array}{l} 0 if i \neq j; \\ 1 if i = j. \end{array}\right.$

The stiffness matrix is given as $K_T = [K_{HS} + K_M]$, consisting of hydrostatic and mooring line stiffness, presented as a combined 6x6 matrix as in equations below. Components of the hydrostatic stiffness matrix are given in Table 6.

**Table 5**
Components of FPSO added mass matrix [28].

| $m_{ij}$ | Formula |
|---|---|
| $m_{11}$ | $km_{11}$ |
| $m_{22}$ | $\mu_1\lambda\frac{\rho\pi}{2}\int_{L_1}^{L_2}T(x)^2k_{22}(x)dx$ |
| $m_{24}, m_{42}$ | $\mu_1\lambda\frac{\rho}{2}\int_{L_1}^{L_2}T(x)^3k_{24}(x)dx$ |
| $m_{26}, m_{62}$ | $\mu_2\lambda\frac{\rho\pi}{2}\int_{L_1}^{L_2}T(x)^2k_{22}(x)xdx$ |
| $m_{33}$ | $\mu_1\lambda\frac{\rho\pi}{8}\int_{L_1}^{L_2}B(x)^2k_{33}(x)dx$ |
| $m_{13}, m_{31}$ | 0 |
| $m_{35}, m_{53}$ | $-\mu_2(\lambda=\frac{L}{8})\frac{\rho\pi}{8}\int_{L_1}^{L_2}B(x)^2k_{33}(x)xdx$ |
| $m_{44}$ | $-\mu_1\lambda\frac{\rho\pi}{256}\int_{L_1}^{L_2}B(x)^4k_{44}(x)dx$ |
| $m_{55}$ | $k_{44}I_{yy}$ |
| $m_{46}, m_{64}$ | $\mu_1\lambda\frac{\rho\pi}{2}\int_{L_1}^{L_2}T(x)^3k_{24}(x)xdx$ |
| $m_{15}, m_{51}$ | $m_{15} = m_{51} = -m_{11}\frac{m_{42}}{m_{22}}$ |
| $m_{66} = \int_{L_1}^{L_2}m_{66}(x)dx$ | $\mu_2\lambda\frac{\rho\pi}{2}\int_{L_1}^{L_2}T(x)^2k_{22}(x)x^2dx$ |

**Table 6**
Components of hydrostatic stiffness matrix.

| $K_{ij}$ | Formula |
|---|---|
| $K_{33}$ | $\rho gS_{wp}$ |
| $K_{34}$ | $\rho g\iint_{S_{bo}}yn_3ds$ |
| $K_{35}$ | $-\rho g\iint_{S_{bo}}xn_3ds$ |
| $K_{43}$ | $K_{43} = K_{34}$ |
| $K_{44}$ | $\rho g\bar{V}G_{M4}$ |
| $K_{45}$ | $-\rho g\iint_{S_{bo}}xyn_3ds$ |
| $K_{46}$ | $-\rho g\bar{V}x_b \mp Wx_g$ |
| $K_{53}$ | $K_{53} = K_{35}$ |
| $K_{54}$ | $K_{54} = K_{45}$ |
| $K_{55}$ | $\rho g\bar{V}G_{M5}$ |
| $K_{56}$ | $-\rho g\bar{V}y_b + Wy_g$ |

$$K_{HS} = \begin{bmatrix} 0 & 0 & 0 & 0 & 0 & 0 \\ 0 & 0 & 0 & 0 & 0 & 0 \\ 0 & 0 & K_{33} & K_{34} & K_{35} & 0 \\ 0 & 0 & K_{43} & K_{44} & K_{45} & K_{46} \\ 0 & 0 & K_{53} & K_{54} & K_{55} & K_{46} \\ 0 & 0 & 0 & 0 & 0 & 0 \end{bmatrix} \tag{28}$$

$$K_m = \begin{bmatrix} K_{11} & 0 & 0 & 0 & K_{15} & 0 \\ 0 & K_{22} & 0 & K_{24} & 0 & 0 \\ 0 & 0 & K_{33} & 0 & 0 & 0 \\ 0 & K_{42} & 0 & K_{44} & 0 & 0 \\ K_{51} & 0 & 0 & 0 & K_{55} & 0 \\ 0 & 0 & 0 & 0 & 0 & K_{66} \end{bmatrix} \tag{29}$$

where; $K_{11} = K_{22} = \frac{4T}{L}$, $K_{24} = K_{42} = -K_{15} = -K_{51} = \frac{4TD}{L}$, $K_{33} = 4K_I$, $K_{55} = K_{44} = \frac{4TD^2}{L} + 2K_I R^2 + 4TD$, $K_{44} = \frac{4TR^2}{L}$ , **T** is the tension in the line pretension caused by excess buoyancy and **L** is the stretched cable length.

Damping coefficient matrix is as presented in Eq. (30),

$$C = \begin{bmatrix} 0 & 0 & 0 & 0 & 0 & 0 \\ 0 & C_{22} & 0 & C_{24} & 0 & C_{26} \\ 0 & 0 & C_{33} & 0 & C_{35} & 0 \\ 0 & C_{42} & 0 & C_{44} & 0 & C_{46} \\ 0 & 0 & C_{53} & 0 & C_{55} & 0 \\ 0 & C_{62} & 0 & C_{64} & 0 & C_{66} \end{bmatrix} \tag{30}$$

where,$c_{jk}$ and $m_{jk}$ are the two-dimensional damping coefficient and added mass for each FPSO strip section, $x_T$ is the coordinate of the transom stern, the integration performed along the length L. Component of the damping matrix are presented as given by [30].

$$C_{22} = \int_L c_{22}(x)dx + Um_{22}(x_T), C_{24} = \int_L c_{24}(x)dx + Um_{24}(x_T)$$

$$C_{26} = \int_L xc_{22}(x)dx + U\int_L m_{22}(x)dx + Ux_T m_{22}(x_T) - \frac{U^2}{\omega_e{}^2}c_{22}(x_T)$$

$$C_{33} = \int_L c_{33}(x)dx + Um_{33}(x_T)$$

$$C_{35} = -\int_L xc_{33}(x)dx - U\int_L m_{33}(x)dx - Ux_T m_{33}(x_T) + \frac{U^2}{\omega_e{}^2}c_{33}(x_T)$$

$$C_{42} = \int_L c_{24}(x)dx + Um_{24}(x_T), C_{44} = \int_L c_{44}(x)dx + Um_{44}(x_T)$$

$$C_{46} = \int_L xc_{24}(x)dx + U\int_L m_{24}(x)dx + Ux_T m_{24}(x_T) - \frac{U^2}{\omega_e{}^2}c_{24}(x_T)$$

$$C_{53} = -\int_L xc_{33}(x)dx + U\int_L m_{33}(x)dx - Ux_T m_{33}(x_T)$$

$$C_{55} = \int_L x^2 c_{33}(x)dx + \frac{U^2}{\omega_e{}^2}\int_L m_{33}(x)dx + Ux^2{}_T m_{33}(x_T) - \frac{U^2}{\omega_e{}^2}c_{33}(x_T)$$

$$C_{62} = -\int_L xc_{22}(x)dx - U\int_L m_{22}(x)dx + Ux_T m_{22}(x_T)$$

$$C_{64} = \int_L xc_{24}(x)dx - U\int_L m_{24}(x)dx + Ux_T m_{24}(x_T)$$

$$C_{66} = \int_L x^2 c_{22}(x)dx + \frac{U^2}{\omega_e{}^2}\int_L m_{22}(x)dx + Ux^2{}_T m_{22}(x_T) - \frac{U^2}{\omega_e{}^2}c_{22}(x_T)$$

The platform response is determined by solving the equation of motion using the two-stage predictor-corrector numerical analysis scheme.

Given the time domain global equation of motion as:

$$\mathbf{F}_t = MA \tag{31}$$

where **M** is the assembled structural and added mass matrix, **A**, the unknown acceleration vector and $\mathbf{F}_t$, the total applied force vector.$\mathbf{F}_t$ is first computed as a function of the known time, position and velocity. **A** is then solved using Eq. (31), the predicted velocity and position at time $t + dt$ are given respectively as:

$$\mathbf{V}^*(t+dt) = \mathbf{V}(t) + \mathbf{A}(t)dt \tag{32}$$

$$\mathbf{X}^*(t+dt) = \mathbf{X}(t) + \mathbf{V}(t)dt + \mathbf{A}(t)\frac{dt^2}{2} \tag{33}$$

In the second stage, the total applied force $\mathbf{F}_t^*$ is estimated at time $t + dt$. The estimated acceleration $\mathbf{A}^*$ is solved using Eq. (31), and the corrected velocity and position at time $t + dt$ are given respectively using Taylor's theorem:

$$\mathbf{V}(t+dt) = \mathbf{V}(t) + \frac{\mathbf{A}(t) + \mathbf{A}^*(t+dt)}{2}dt \tag{34}$$

$$\mathbf{X}(t+dt) = \mathbf{X}(t) + \mathbf{V}(t)dt + \frac{2\mathbf{A}(t) + \mathbf{A}^*(t+dt)}{6}dt^2 \tag{35}$$

## 4. Results and discussions

### 4.1. Static offset

In order to match the surge mooring line restoring forces for the cases considered, the static offset of the systems is made to match as close as possible for all tested depths. Fig. 4 shows the results for diameter, D = 156 mm, which agrees well for the tested depths. Cases of D = 201 mm, 251 mm and 290 mm were also conducted and results are found to agree well among each other.

### 4.2. Effect of mooring line diameter

Coupled dynamic analyses were conducted for various polyester segment diameter, i.e. D = 156 mm, 201 mm, 251 mm and 290 mm, at 1000 m and 2000 m water depths. The chain segment properties remain the same for all cases considered.

Figs. 5, 6 and Table 7 show the surge spectrum and the statistical values for 1000 m and 2000 m water depth for various mooring line diameters, i.e. 156 mm, 201 mm, 251 mm, 290 mm. Figs. 5 and 6 show dominant low frequency surge motion. Also, a significant reduction in the surge response corresponding to the increase in mooring line diameter was observed. Table 7 shows a reduction of the Standard Deviation (S.D) and the maximum surge spectrum response corresponding to the increase in mooring line diameter. This is due to higher mooring line damping possessed by larger line diameters; however, their effect is observed to decrease as the diameter increases.

At 2000 m water depth, the surge spectrum and statistical values of D = 251 mm and 290 mm were relatively observed to be equal. A reduction in the maximum surge was recorded for up to

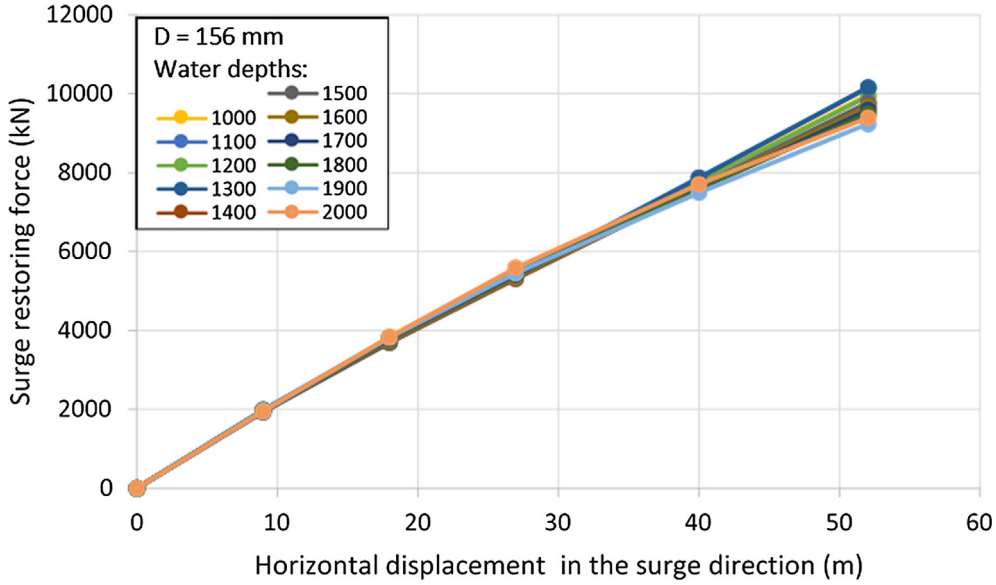


**Fig. 4.** Surge static offset (D = 156 mm).

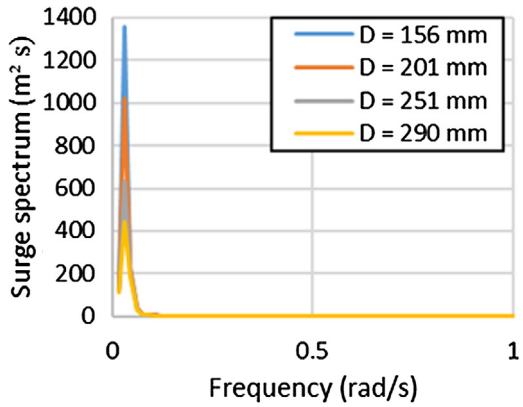


**Fig. 5.** Surge spectrum (1000 m).

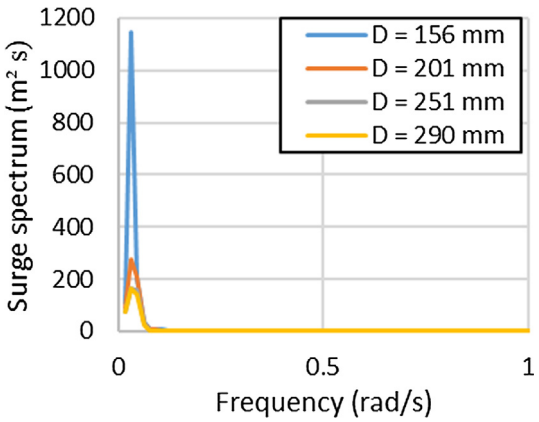


**Fig. 6.** Surge spectrum (2000 m).

54% from diameter 156 mm to 201 mm, 32% from mooring line diameter 201 mm to 251 mm, and 14% from diameters 251 mm to 290 mm respectively. This implies that at deeper waters, increasing the mooring line diameter past a certain range will not have any significant effect on the surge motions.

**Table 7**
Surge statistical values (in m).

| | | D = 156 mm | D = 201 mm | D = 251 mm | D = 290 mm |
|---|---|---|---|---|---|
| Depth = 1000 m | max | 10.7 | 10.32 | 8.1 | 6.37 |
| | min | −20.54 | −20.79 | −20 | −19.39 |
| | mean | −4.63 | −4.55 | −4.57 | −4.57 |
| | s.d. | 5.33 | 4.86 | 4.1 | 3.62 |
| Depth = 2000 m | max | 9.6 | 4.38 | 2.96 | 2.54 |
| | min | −19.08 | −18.08 | −16.84 | −16.75 |
| | mean | −4.51 | −4.55 | −4.51 | −4.49 |
| | s.d. | 4.96 | 3.23 | 2.73 | 2.67 |

Table 8 shows no significant changes for the heave, roll and pitch, which is due to the fact that these motions are primarily governed by the structural damping of the hull and the contribution of mooring line stiffness is small in these motions. Due to their natural frequencies close to the typical ocean waves' frequencies, the three motions are wave frequency (WF) dominated. Hence, WF-dominated motions of heave, pitch and roll are largely unaffected by mooring line diameter at both 1000 m and 2000 m water depth as shown in Table 9.

The mooring line tensions of line group G3 at 1000 m and 2000 m as in Figs. 7 and 8 show a reduction in tension spectrum with increasing line diameter in the dominated Lower Frequency (LF) region, which is similar to the surge spectrum.

### 4.3. Effect of water depth

The analysis was conducted using polyester mooring line diameters, i.e. D = 156 mm, 201 mm, 256 mm and 290 mm, and simulations carried out at water depths ranging from 1000 m to 2000 m, at 100 m intervals, for each mooring line diameter. The peak points of the spectrum were presented for comparison between the surge and line tension. The statistical data are presented in Tables 10 and 11.

A general decrease in peak surge responses for all mooring line diameters at all water depths were observed in Fig. 9. However, for mooring line diameter 156 mm, the decrease was relatively linear in trend up to 1400 m water depth, after which a sudden increase in the peak surge value was recorded from 1400 m to 1500 m

**Table 8**
Heave, roll, and pitch statistical values.

| Motion | Depth | | D = 156 mm | D = 201 mm | D = 251 mm | D = 290 mm |
|---|---|---|---|---|---|---|
| Heave (m) | 1000 | max | 8.21 | 8.22 | 8.27 | 8.28 |
| | | min | −9.82 | −9.91 | −9.91 | −9.91 |
| | | mean | −0.09 | −0.09 | −0.09 | −0.10 |
| | | s.d. | 2.35 | 2.37 | 2.38 | 2.39 |
| | 2000 | max | 8.09 | 8.14 | 8.16 | 8.16 |
| | | min | −9.95 | −9.82 | −9.88 | −9.98 |
| | | mean | −0.23 | −0.13 | −0.15 | −0.19 |
| | | s.d. | 2.36 | 2.35 | 2.36 | 2.38 |
| Roll (rad) | 1000 | max | 0.01668 | 0.01499 | 0.01486 | 0.01465 |
| | | min | −0.01677 | −0.01403 | −0.01351 | −0.01373 |
| | | mean | 0.00015 | 0.00015 | 0.00015 | 0.00015 |
| | | s.d. | 0.00419 | 0.00383 | 0.00378 | 0.00378 |
| | 2000 | max | 0.01417 | 0.01451 | 0.01583 | 0.01568 |
| | | min | −0.01390 | −0.01403 | −0.01539 | −0.01533 |
| | | mean | 0.00015 | 0.00015 | 0.00015 | 0.00015 |
| | | s.d. | 0.00365 | 0.00384 | 0.00396 | 0.00383 |
| Pitch (rad) | 1000 | max | 0.07422 | 0.07482 | 0.07488 | 0.07488 |
| | | min | −0.06428 | −0.06400 | −0.06422 | −0.06429 |
| | | mean | 0.00193 | 0.00195 | 0.00196 | 0.00199 |
| | | s.d. | 0.01777 | 0.01787 | 0.01794 | 0.01798 |
| | 2000 | max | 0.07501 | 0.07442 | 0.07477 | 0.07534 |
| | | min | −0.06361 | −0.06397 | −0.06397 | −0.06387 |
| | | mean | 0.00279 | 0.00216 | 0.00232 | 0.00251 |
| | | s.d. | 0.01785 | 0.01775 | 0.01783 | 0.01792 |

**Table 9**
Tension G3 statistical values (in kN).

| | | D = 156 mm | D = 201 mm | D = 251 mm | D = 290 mm |
|---|---|---|---|---|---|
| Depth = 1000 m | max | 5072.14 | 5106.77 | 5365.6 | 5280.52 |
| | min | 519.98 | 538.13 | 793.37 | 1038.38 |
| | mean | 2380.32 | 2433.15 | 2485.57 | 2593.67 |
| | s.d. | 757.8 | 683.45 | 601.43 | 546.38 |
| Depth = 2000 m | max | 6526.56 | 5411.68 | 5468.37 | 6117.35 |
| | min | 3098.31 | 1357.16 | 2126.01 | 2723.15 |
| | mean | 4728.18 | 3046.59 | 3551.21 | 4142 |
| | s.d. | 560.48 | 540.78 | 454.88 | 438.69 |

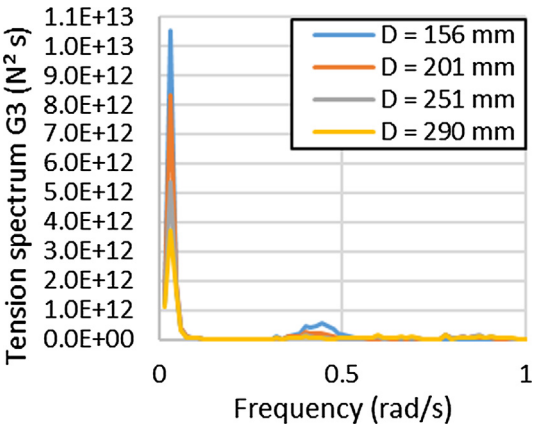


**Fig. 7.** Tension spectrum G3 (depth = 1000 m).

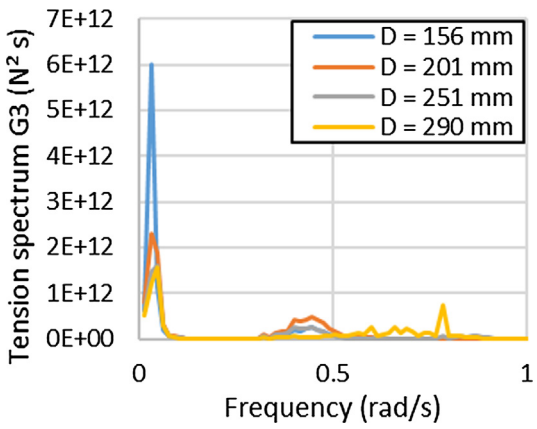


**Fig. 8.** Tension spectrum G3 (depth = 2000 m).

before resuming the normal decreasing trend. This is probably due to the significant "jump" in pretension from 1400 m to 1500 m, which is necessary to maintain the surge mooring line restoring force in the static offset as shown in Table 12. Subsequent percentage increase in pretension at water depth intervals is less than 7% from water depth 1000 m to 1400 m, at 1500 m, the pretension increment was 28%, which is four times greater than the previous increment recorded. For water depth between 1500 m and 2000 m, the increase was less than 17%. This will also be in agreement with the trend of surge maximum and S.D values when plotted using Table 10.

Unlike D = 156 mm, the surge responses of the other three mooring line diameters displayed more consistent decreasing trend. The decrease is most significant at lower water depths (between 1000 and 1500 m) but becomes less pronounced at deeper waters (greater than1500 m). In addition, maximum and S.D values were observed to decrease, as shown in Table 10; the rate of decrease also becoming smaller the greater the depth.

**Table 10**
Surge statistical results.

| Diameter | | 1000 | 1100 | 1200 | 1300 | 1400 | 1500 |
|---|---|---|---|---|---|---|---|
| 156 mm | max | 10.7 | 10.25 | 10.06 | 9.63 | 9.62 | 10.64 |
| | min | −20.54 | −20.24 | −20.29 | −20.18 | −20.18 | −20.1 |
| | mean | −4.63 | −4.62 | −4.57 | −4.65 | −4.51 | −4.6 |
| | s.d. | 5.33 | 5.13 | 4.95 | 4.8 | 4.71 | 5.4 |
| 201 mm | max | 10.32 | 9.77 | 8.78 | 8.35 | 7.14 | 6.21 |
| | min | −20.79 | −20.68 | −20.25 | −20.18 | −19.57 | −19.29 |
| | mean | −4.55 | −4.6 | −4.63 | −4.58 | −4.52 | −4.55 |
| | s.d. | 4.86 | 4.63 | 4.3 | 4.11 | 3.87 | 3.71 |
| 251 mm | max | 8.1 | 7.06 | 6.08 | 5.46 | 4.57 | 4.02 |
| | min | −20 | −19.68 | −19.28 | −18.87 | −18.37 | −18.1 |
| | mean | −4.57 | −4.56 | −4.55 | −4.49 | −4.52 | −4.53 |
| | s.d. | 4.1 | 3.78 | 3.54 | 3.39 | 3.17 | 3.07 |
| 290 mm | max | 6.37 | 5.45 | 4.59 | 3.92 | 3.24 | 2.87 |
| | min | −19.39 | −18.95 | −18.4 | −18.06 | −17.61 | −17.47 |
| | mean | −4.57 | −4.52 | −4.5 | −4.5 | −4.47 | −4.5 |
| | s.d. | 3.62 | 3.37 | 3.17 | 3.02 | 2.89 | 2.84 |
| Diameter | | 1600 | 1700 | 1800 | 1900 | 2000 | |
| 156 mm | max | 10.51 | 10.29 | 10.22 | 9.98 | 9.6 | |
| | min | −19.91 | −19.64 | −19.53 | −19.35 | −19.08 | |
| | mean | −4.54 | −4.53 | −4.5 | −4.48 | −4.51 | |
| | s.d. | 5.28 | 5.21 | 5.16 | 5.05 | 4.96 | |
| 201 mm | max | 5.76 | 5.39 | 5.03 | 4.81 | 4.38 | |
| | min | −18.96 | −18.75 | −18.55 | −18.24 | −18.08 | |
| | mean | −4.53 | −4.54 | −4.56 | −4.51 | −4.55 | |
| | s.d. | 3.57 | 3.46 | 3.37 | 3.32 | 3.23 | |
| 251 mm | max | 3.47 | 3.27 | 3.23 | 3.15 | 2.96 | |
| | min | −17.66 | −17.4 | −17.23 | −17.08 | −16.84 | |
| | mean | −4.5 | −4.5 | −4.5 | −4.5 | −4.51 | |
| | s.d. | 2.96 | 2.87 | 2.84 | 2.8 | 2.73 | |
| 290 mm | max | 2.62 | 2.59 | 2.56 | 2.48 | 2.54 | |
| | min | −17.2 | −17.02 | −16.87 | −16.74 | −16.75 | |
| | mean | −4.51 | −4.49 | −4.48 | −4.48 | −4.49 | |
| | s.d. | 2.73 | 2.71 | 2.68 | 2.65 | 2.67 | |

**Table 11**
Statistical results of tension G3.

| Diameter | | 1000 | 1100 | 1200 | 1300 | 1400 | 1500 |
|---|---|---|---|---|---|---|---|
| 156 mm | max | 5072.14 | 5060.03 | 5077 | 5095.4 | 5125 | 5673.5 |
| | min | 519.98 | 436.89 | 498.33 | 499.4 | 633.75 | 1635.41 |
| | mean | 2380.32 | 2369.97 | 2434.5 | 2408.03 | 2562.78 | 3249.09 |
| | s.d. | 757.8 | 755.82 | 727.35 | 722.88 | 683.01 | 698.3 |
| 201 mm | max | 5106.77 | 4918.93 | 5113.39 | 4908.16 | 5044.15 | 5175.49 |
| | min | 538.13 | 566.68 | 573.69 | 648.37 | 804.25 | 931.4 |
| | mean | 2433.15 | 2457.32 | 2443.31 | 2535.16 | 2623.32 | 2676.57 |
| | s.d. | 683.45 | 654.41 | 638.51 | 609.94 | 582.84 | 570.31 |
| 251 mm | max | 5365.6 | 5278.22 | 5246.74 | 5198.53 | 5155.09 | 5127.91 |
| | min | 793.37 | 836.96 | 941.01 | 1109.1 | 1165.38 | 1308.61 |
| | mean | 2485.57 | 2548.57 | 2641.52 | 2788.27 | 2839.46 | 2958.54 |
| | s.d. | 601.43 | 568.89 | 538.63 | 515.41 | 497.81 | 482.38 |
| 290 mm | max | 5280.52 | 5334.5 | 5425 | 5566.4 | 5647.52 | 5742.33 |
| | min | 1038.38 | 1188.92 | 1320.53 | 1454.55 | 1611.5 | 1786.54 |
| | mean | 2593.67 | 2732.84 | 2860.7 | 2989.48 | 3131.68 | 3291.72 |
| | s.d. | 546.38 | 518.76 | 498.22 | 490.51 | 472.65 | 466.68 |
| Diameter | | 1600 | 1700 | 1800 | 1900 | 2000 | |
| 156 mm | max | 6006.84 | 6445.32 | 6655.91 | 6356.08 | 6526.56 | |
| | min | 2116.82 | 2704.95 | 3019.05 | 2772.13 | 3098.31 | |
| | mean | 3757.2 | 4339.99 | 4659.82 | 4448.04 | 4728.18 | |
| | s.d. | 658.53 | 627.27 | 606.96 | 588.06 | 560.48 | |
| 201 mm | max | 5225.22 | 5204.87 | 5314.6 | 5375.48 | 5411.68 | |
| | min | 1047.52 | 1103.11 | 1152.82 | 1291.54 | 1357.16 | |
| | mean | 2750.34 | 2816.45 | 2885.46 | 3006.44 | 3046.59 | |
| | s.d. | 561.14 | 555.05 | 550.16 | 540.22 | 540.78 | |
| 251 mm | max | 5186.78 | 5256.67 | 5346.56 | 5437.87 | 5468.37 | |
| | min | 1462.46 | 1601.34 | 1793.96 | 1963.4 | 2126.01 | |
| | mean | 3079.64 | 3185.13 | 3332.87 | 3463.46 | 3551.21 | |
| | s.d. | 471.78 | 466.23 | 457.27 | 452.48 | 454.88 | |
| 290 mm | max | 5782.5 | 5854.5 | 5944.57 | 5995.79 | 6117.35 | |
| | min | 1915.57 | 2117.49 | 2323.76 | 2502.13 | 2723.15 | |
| | mean | 3396.13 | 3588.42 | 3770.46 | 3927.79 | 4142 | |
| | s.d. | 455.09 | 453.52 | 446.04 | 442.1 | 438.69 | |

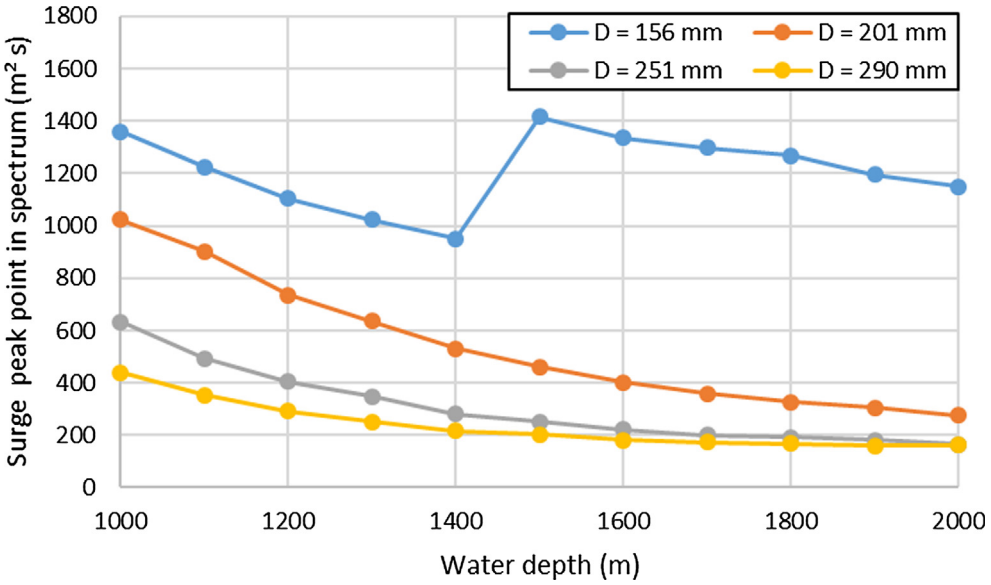


**Fig. 9.** Surge peak point in the spectrum.

**Table 12**
Mooring line pretension.

| | | | | | | | |
|---|---|---|---|---|---|---|---|
| Water depth | Units | 1000 | 1100 | 1200 | 1300 | 1400 | 1500 |
| Pretension | kN | 589 | 585 | 612 | 601 | 644 | 896 |
| Water depth | | 1600 | 1700 | 1800 | 1900 | 2000 | |
| Pretension | kN | 1078 | 1283 | 1397 | 1330 | 1429 | |

No significant changes were observed in the mean surge of all the scenarios considered; hence it is concluded that the water depth does not significantly affect the mean surge motion. Fig. 10 shows a plot of peak tension spectrum of G3 mooring line.

A general decrease linearly with increasing water depth was recorded for D = 156 mm, which shows a similar trend with the previously discussed surge response. On the other hand, the maximum, minimum and mean tension were observed to increase significantly from water depths of 1400–1800 m, which is also connected with the increase in pretension as shown in Fig. 12. The difference in pretension is less than 50 kN for each subsequent 100 m depth interval from 1000 m to 1400 m. From 1400 m to 1800 m however, the pretension increases by more than 100 kN for each 100 m depth increase. The statistical values for D = 156 mm show strong agreement with the previous Figs. 9 and 10. Also, the tension S.D. for D = 156 mm, when observed from Table 11, generally decreases in a relatively more linear fashion, with the jump at 1500 m much less pronounced.

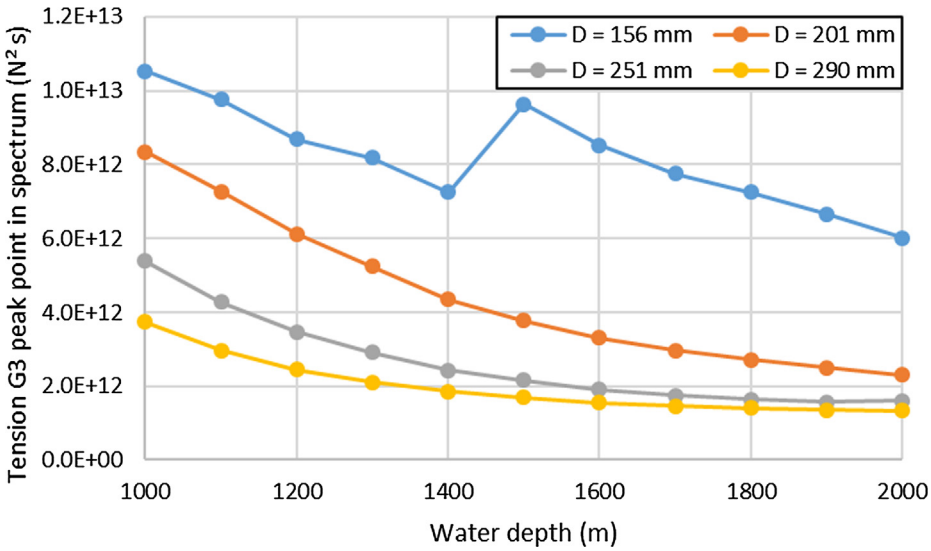


**Fig. 10.** Tension G3 peak point in the spectrum.

**Table 13**
Tension G3 statistical values (in kN).

| Parameter | Units | Value | | | |
|---|---|---|---|---|---|
| | | Case 1a | Case 1b | Case 2a | Case 2b |
| Diameter | mm | 156 | 156 | 290 | 290 |
| Normal drag coefficient, $C_{DN}$ | – | 1.2 | 2 | 1.2 | 2 |
| Normal added inertia coefficient, $C_{IN}$ | – | 1.1 | 2 | 1.1 | 2 |

In contrast to D = 156 mm, the line tension peak spectrum points for D = 201 mm, 251 mm, and 290 mm decrease in a non-linear fashion. A similar trend is also observed for the corresponding S.D values, while the mean tensions generally increase linearly with increasing depth. Interestingly, the correlation between the maximum tension value with the pretension for D = 201 and 251 mm appear to weaken compared to D = 156 mm. This might be attributed to the geometric state of the mooring lines. When D = 156 mm, the lines are taut, and the dynamic effects are said to be minimal. However, the remaining three diameters are generally found to be less taut, particularly at greater water depths. Hence greater dynamic effects are expected. This can be anticipated from the significantly lower line pretension required to maintain the surge mooring line restoring force (see Table 3), and later proven by the greater significance of the WF component relative to the overall spectrum, as previously found in Fig. 8. Thus the maximum tension response trend becomes more complex to predict for D = 201 mm, 251 mm, and 290 mm.

### 4.4. Effect of drag and added inertia coefficients

To investigate the significance of mooring line drag and added inertia, the two coefficients from the previous simulations are increased for the polyester segments, as shown in Table 13. The four cases are simulated at 2000 m water depths. Case 1a and Case 2a are the original simulations found in the previous section. All other parameters, e.g., line length, line weight, pretension, etc. remain the same.

Figs. 11–14 show the surge and mooring line spectrum. It is observed that, the LF surge motion and mooring tension reduces with the increase of the hydrodynamic coefficients. Table 14 show the statistical parameters for the 6 DOF in addition to mooring line tension (G3). Only the max. LF surge motion and mooring tension, which is primarily given by surge, reduce by increasing the hydrodynamic coefficients while there is no much change in the other DOF. This is due to the fact that the mooring line damping reduces the LF responses only, which in this case is the surge motions and mooring line tension.

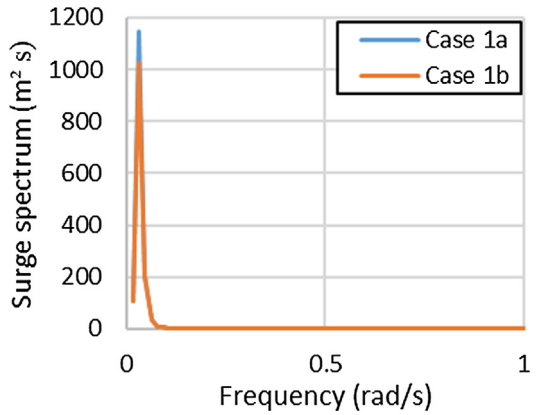


**Fig. 11.** Surge spectrum (D = 156 mm).

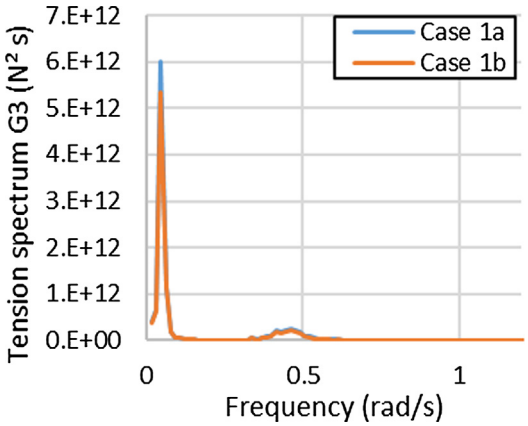


**Fig. 13.** Tension spectrum G3 (D = 156 mm).

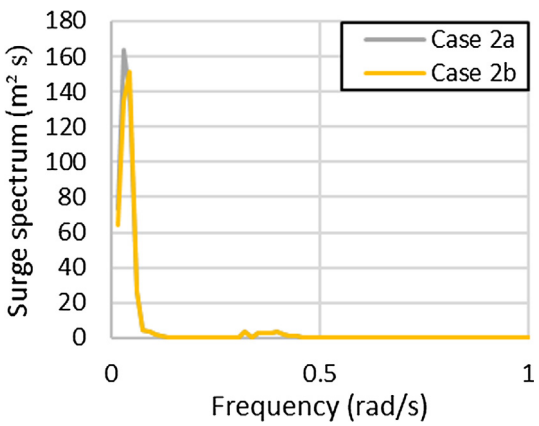


**Fig. 12.** Surge spectrum (D = 290 mm).

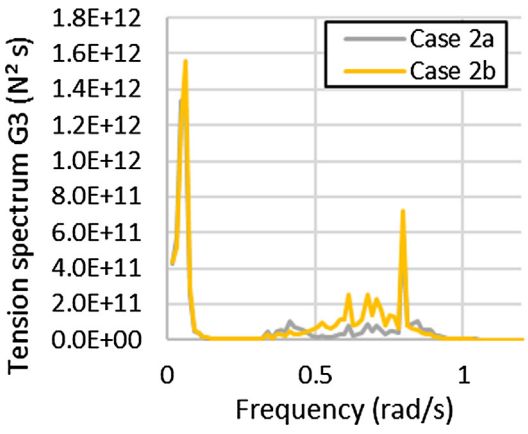


**Fig. 14.** Tension spectrum G3 (D = 290 mm).

**Table 14**
Summary of statistical results.

| | | Case 1a | Case 1b | Case 2a | Case 2b |
|---|---|---|---|---|---|
| Surge (m) | max | 9.60 | 9.25 | 2.54 | 2.47 |
| | min | −19.08 | −19.13 | −16.75 | −16.28 |
| | mean | −4.51 | −4.51 | −4.49 | −4.49 |
| | s.d. | 4.96 | 4.76 | 2.67 | 2.59 |
| Heave (m) | max | 8.09 | 8.10 | 8.16 | 8.19 |
| | min | −9.95 | −9.96 | −9.98 | −10.02 |
| | mean | −0.23 | −0.23 | −0.19 | −0.19 |
| | s.d. | 2.36 | 2.37 | 2.38 | 2.39 |
| Roll (rad) | max | 0.01417 | 0.01447 | 0.01568 | 0.01530 |
| | min | −0.01390 | −0.01418 | −0.01533 | −0.01497 |
| | mean | 0.00015 | 0.00015 | 0.00015 | 0.00015 |
| | s.d. | 0.00365 | 0.00370 | 0.00383 | 0.00371 |
| Pitch (rad) | max | 0.07501 | 0.07509 | 0.07534 | 0.07555 |
| | min | −0.06361 | −0.06369 | −0.06387 | −0.06400 |
| | mean | 0.00279 | 0.00279 | 0.00251 | 0.00251 |
| | s.d. | 0.01785 | 0.01786 | 0.01792 | 0.01798 |
| G3 (kN) | max | 6527 | 6512 | 6117 | 6225 |
| | min | 3098 | 3147 | 2723 | 2655 |
| | mean | 4728 | 4728 | 4142 | 4142 |
| | s.d. | 560 | 537 | 439 | 488 |

## 5. Conclusion

A study was conducted to investigate the effects of water depth, mooring line diameter as well as drag and added inertia coefficients on the dynamic motions and mooring line tensions of FPSO platform in deep waters using coupled dynamic analysis. Based on the results, the following conclusions can be drawn:

- The surge motion is governed by LF responses, mainly influences by mooring line diameter which affects the mooring line damping. For relatively deep waters, the effect of mooring line diameter is insignificant beyond certain range. The effect of mooring dimeter on the mooring line tension is similar to its effect on surge motion response.
- Water depth affects the surge response, particularly the LF motions. This is due to the increase in the mooring line length which adds to the mooring line damping. The similar trend has been observed in mooring line tensions.
- As the hydrodynamic coefficients influence the mooring line damping, which decreases the LF motions and tensions, only surge motion and mooring line tensions affected by changing these coefficients.

## Declaration of Competing Interest

The authors declare that they have no known competing financial interests or personal relationships that could have appeared to influence the work reported in this paper.

## Acknowledgement

The Ministry of Education (MOE), Malaysia is gratefully acknowledged for funding this research under the FRGS Grant (0153AB-K87).

## References

[1] Arvind K. Appraisal of riser concepts for FPSO in deepwater. MSc, Marine and Subsea Technology, University of Stavanger, Faculty of Science and Technology; 2014.
[2] Offshore M. Available floating production units (FPU) count at all-time high. Offshore Magazine; 2013. Available: https://www.offshore-mag.com/rigs-vessels/article/16771624/available-fpu-count-at-alltime-high.
[3] Kim BW, Sung HG, Kim JH, Hong SY. Comparison of linear spring and nonlinear FEM methods in dynamic coupled analysis of floating structure and mooring system. J Fluids Struct 2013;42:205.
[4] Soares CG, Fonseca N, Pascoal R. Experimental and numerical study of the motions of a turret moored fpso in waves. J Offshore Mech Arct Eng 2004;127:197–204.
[5] Chen X, Zhang J, Ma W. On dynamic coupling effects between a spar and its mooring lines. Ocean Eng 2001;28:863–87.
[6] Bergdahl LM, Rask I. Dynamic vs. quasi-static design of catenary mooring system. In: 19th offshore technology conference, Houston; 1987.
[7] Inoue Y, Miyabe H, Weiyi X, Nakamura M. Comparative study on the quasi-static analyses and dynamic simulations for estimating the maximum tensions of mooring lines. In: 1st international offshore and polar engineering conference, Edinburgh; 1991.
[8] Ormberg H, Larsen K. Coupled analysis of floater motion and mooring dynamics for a turret-moored ship. Appl Ocean Res 1988;20:55–67.
[9] A. Tahar, Z. Ran, and M. Kim, "Hull/mooring/riser coupled spar motion analysis with buoyancy-can effect," in 12th International Offshore and Polar Engineering Conference, Kitakyushu, 2002.
[10] Luo Y, Baudic S. Predicting FPSO responses using model tests and numerical analysis. In: 13th international offshore and polar engineering conference, Honolulu; 2003.
[11] Wichers JEW, Huijsmans RHM. The contribution of hydrodynamic damping induced by mooring chains on low-frequency vessel motions. In: 22nd offshore technology conference, Houston; 1990.
[12] Chen X. Studies on dynamic interaction between deep-water floating structures and their mooring/tendon systems, PhD PhD, Department of Ocean Engineering. Texas: Texas A&M University; 2002.
[13] Ran Z. Coupled dynamic analysis of floating structures in waves and currents. PhD PhD thesis, Offshore Technology Research Center, Department of Ocean Engineering, Texas A&M University, Texas; 2000.
[14] Arcandra and A. university, Hull/mooring/riser coupled dynamic analysis of a deepwater floating platform with polyester lines, Texas A&M University; 2001.
[15] Young-Bok K. Dynamic analysis of multiple-body floating platforms coupled with mooring lines and risers. PhD, Ocean Engineering, Texas A&M University, Texas University; 2003.
[16] Lin Z, Sayer P. Influence of water depth variation on the hydrodynamics of deep-water mooring characteristics. Ocean Eng 2015;109:553–66.
[17] Aage C, Bernitsas MM, Choir HS, Crudu I, Incecik I, Murray JJ. The specialist committee on deep water mooring:final report and recommendations to the 22nd ITTC. International towing tank conference, Seoul, 2000.
[18] Guan1 M, M.O, Ng CY. Prediction of deepwater FPSO responses using different numerical analysis methods. E3S Web of Conferences, 2018.
[19] Low Y, Langley R. Time and frequency domain coupled analysis of deepwater floating production systems. Appl Ocean Res 2006;28:371–85.
[20] Qiao D, Li B, Ou J. Comparative analysis on coupling effects between an innovative deep draft platform and different mooring models. Brodogradnja 2012;63:313–28.
[21] Kinoshita T, Hirata K, Colbourne B, Pinkster JA, Jianmin Y, Ha MK, et al. Report of the ITTC specialist committee on stationary floating systems. In: 23rd international towing tank conference ITTC. p. 545–71.
[22] Lin Z, Sayer PA. Hydrodynamic study of deepwater mooring characteristics. 24th international ocean and polar engineering conference, Busan, 2014.

[23] Heurtier JM, Le Buhan P, Fontaine E, Le Cunff C, Biolley F, Berhault C. Coupled dynamic response of moored FPSO with risers. 11th international offshore and polar engineering conference Stavanger, Norway, 2001.
[24] Montasir OA, Anurag Y, Kurian VJ. Mooring system optimisation and effect of different line design vari-ables on motions of truss spar platforms in intact and damaged condi-tions. China Ocean Eng 2019;33:385–97.
[25] ANSYS.AQWA. ANSYS Help Viewer, v16.2 ed; 2015.
[26] Kim MH, Koo BJ, Mercier RM, Ward EG. Vessel/mooring/riser coupled dynamic analysis of a turret-moored FPSO compared with OTRC experiment. Ocean Eng J 2005;32:1780–802.
[27] Fylling I, Stansberg C. Model testing of deepwater floating production systems: Strategy for truncation of moorings and risers. Deep oil technology, Rio de Janeiro, 2005.
[28] Van den Boom HJJ. Dynamic behaviour of mooring lines. Behav Offshore Struct 1985:359–68.
[29] Sen DT, Vinh TC. Determination of added mass and inertia moment of marine ships moving in 6 degrees of freedom. Int J Transportation Eng Technol 2016;2:8–14.
[30] MARIN, "ANISIM," ed; 2014.

**Dr Montasir Osman** is a Lecturer at Civil Engineering Department, Universiti Teknologi PETRONAS (UTP). He has a total of 13-year experience in Academic Institutions and in Industry. His PhD topic was related to the dynamic analysis of floating offshore structures and mooring line systems. He has about 17 research publications in the same field, in Journals and Conferences. Currently, he is the Head of offshore Laboratory in UTP. He has number of research activities going on related to Hydrodynamics of Floating Platforms', 'Mooring Line analysis: Quasi-static and Dynamic Analysis', 'Wave-wave and Wave-structure Interactions', 'Wave Kinematics and Wave Theories' and 'Wave Directionality'.

**Idris Ahmed Ja'e** is a PhD candidate in the Civil and Engineering Department, UTP. He is pursuing his PhD in offshore Structures, focussing on offshore floating structures and optimisation of mooring lines. He received his BEng in Civil Engineering (2008) from Abubakar Tafawa Balewa University (ATBU), Bauchi-Nigeria, MSc in Civil Engineering (Structures) in 2016 from Ahmadu Bello University (ABU), Zaria-Nigeria.

**Matthew Guan** obtained his Dipl. in Mechanical Engineering at SEGi College in 2011 and B.E. in Civil Engineering at Universiti Teknologi PETRONAS in 2015. He is currently pursuing his MSc in Civil Engineering at UTP. Presently, he is working as a Graduate Research Assistant at the Civil Engineering Department at UTP. His area of research includes Offshore Structures and Mooring Lines.